Solid State Sciences 157 (2024) 107708

Contents lists available at ScienceDirect

Solid State Sciences

journal homepage: www.elsevier.com/locate/ssscie

Tuning conduction properties and clarifying thermoelectric performance of P-type half-heusler alloys $TiNi_{1-x}Co_xSn$ ($0 \leq x \leq 0.15$)

Kosuke Yamazaki [a], Sopheap Sam [b], Yoichi Okamoto [c], Hiroshi Nakatsugawa [a,*]

[a] Yokohama National University, Graduate School of Engineering Science, 79-5 Tokiwadai, Hodogaya, Yokohama, Kanagawa, 240-8501, Japan
[b] National Institute for Materials Science, Namiki 1-1, Tsukuba, Ibaraki, 305-0044, Japan
[c] National Defense Academy, Department of Materials Science and Engineering, 1-10-20 Hashirimizu, Yokosuka, Kanagawa, 239-8686, Japan

ARTICLE INFO

Keywords:
Conduction properties
Thermoelectric performance
P-type
Half-heusler
TiNiSn

ABSTRACT

TiNiSn is an N-type thermoelectric material with a high-power factor composed of low toxicity and abundant elements. TiNiSn also shows P-type electrical conduction by hole doping. In this study, we tune the conduction properties of $TiNi_{1-x}Co_xSn$ ($0 \leq x \leq 0.15$) with Co substitution at the Ni site. The samples were prepared by the arc melting method, and thermoelectric properties were investigated up to 800 K. The results of the Hall effect and the Seebeck coefficient measurements indicate that the majority of charge carriers changes from electrons to holes at $x \geq 0.03$, suggesting that Co acts as an acceptor. We report for the first time that $Ti_{0.994}Ni_{1.00}Co_{0.051}Sn_{1.01}$ exhibits $ZT = 0.12$ at 675 K. This work reveals that $Ti_{0.994}Ni_{1.00}Co_{0.051}Sn_{1.01}$ could be a potential P-type thermoelectric material operating at high temperatures.

1. Introduction

Thermoelectric generators (TEG) can directly convert waste heat into electrical energy. TEG is maintenance-free because there is no driving unit, and it can be used in various environments [1,2]. In addition, power generation does not require fossil fuels and emits carbon dioxide. In general, for thermoelectric conversion modules, efficient thermoelectric conversion can be achieved by using P-type and N-type thermoelectric materials [3,4]. By using thermoelectric materials with a large dimensionless figure of merit, ZT ($=S^2T\rho^{-1}\kappa^{-1}$, where S is Seebeck coefficient, T is temperature, ρ is electrical resistivity, and κ is thermal conductivity, where κ consists of carrier thermal conductivity κ_{el} and lattice thermal conductivity κ_{lat} ($\kappa = \kappa_{el} + \kappa_{lat}$)), the high conversion efficiency can be obtained in the module. Therefore, for practical thermoelectric conversion modules, it is desirable to use thermoelectric materials with large ZT for both P-type and N-type with low environmental effects and low cost. In recent years, many studies on thermoelectric materials have reported the development and performance improvement of eco-friendly, and low-cost thermoelectric materials [5,6], such as oxide [7,8], sulfide [9,10], silicide compounds [11,12], and Heusler alloys [13,14]. Among these materials, the half-Heusler (hH) alloy TiNiSn is chemically stable at high temperatures (up to 1273 K) and has excellent mechanical properties [15], making it suitable for a wide range of environments. It is also an environmentally friendly thermoelectric material because of its non-toxicity and abundant elements [16].

The crystal structure of TiNiSn is MgAgAs type as shown in Fig. 1 (a), where Ti and Sn form a rock salt structure (NaCl), and Ni atoms occupy half of the sublattice. Half of the sublattice is vacancies, but Ni occupies some of the vacancies and tends to form point defects (interstitial atoms) [17]. When the vacancies are completely occupied by Ni atoms, a full Heusler (fH) structure is formed as shown in (b). TiNiSn has a band gap of $E_g \approx 0.45$ eV [18,19], resulting in a large Seebeck coefficient and low electrical resistivity. Therefore, the Power factor $S^2\rho^{-1}$ [$Wm^{-1}K^{-2}$] is large and comparable to that of Bi_2Te_3 [20], a conventional thermoelectric material ($\approx$1.0 $Wm^{-1}K^{-1}$ at room temperature) [21]. One of the ways to improve the performance of thermoelectric materials is to optimize the carrier density using elemental substitution. Our research group has optimized the carrier density by replacing Sn sites with Sb sites and obtained results with improved power factors [22]. TiNiSn exists in the electrical conduction of two types of carriers: electrons and holes. For pristine TiNiSn, the majority of charge carriers are electrons, indicating an N-type electrical conduction [23–25]. On the other hand, when the majority of charge carriers are changed to holes by adding an acceptor, P-type conduction can be obtained [26,27]. The total number of valence electrons (VEC) of the constituent elements is used to control

* Corresponding author.
E-mail address: nakatsugawa-hiroshi-dx@ynu.ac.jp (H. Nakatsugawa).

https://doi.org/10.1016/j.solidstatesciences.2024.107708
Received 28 June 2024; Received in revised form 29 August 2024; Accepted 20 September 2024
Available online 21 September 2024

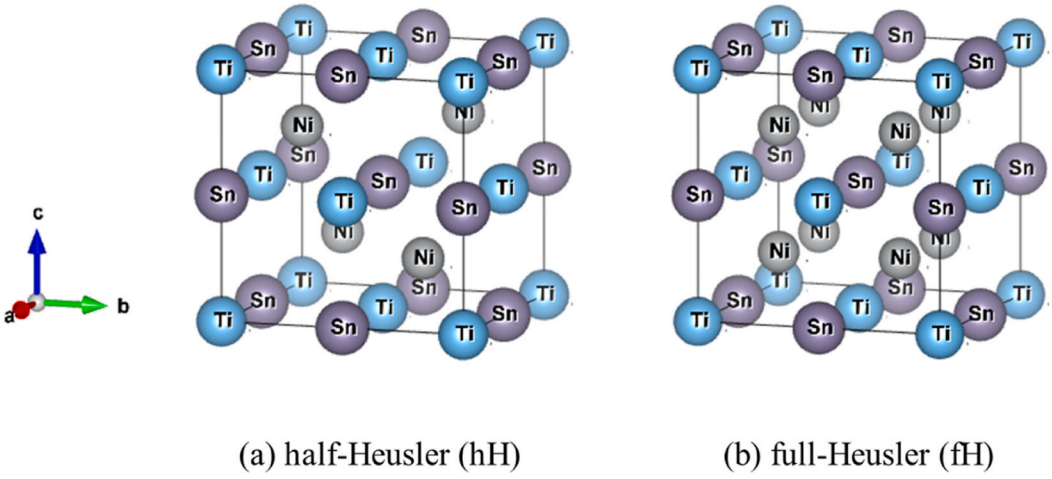

Fig. 1. Crystal structure (a) half-Heusler alloy and (b) full-Heusler alloy.

the majority of charge carriers in half-Heusler alloys (e. g. ZrNiSn [28]) with the band structure having such an energy gap. TiNiSn shows N-type for VEC >18 and P-type for VEC <18.

Other P-type half-Heusler alloys were investigated by many research groups. For example, 6.1 % Ir-doped ZrNiSn had a maximum *ZT* of 0.31 at 100 K [29]. In addition, 25 % Co-doped HfNiSn exhibited a maximum *ZT* of 0.55 at 973 K [30]. It should be noted that those enhanced *ZT* values are mainly contributed by the improvement of power factors ($\approx$1.0–2.0 $mWm^{-1}K^{-2}$). According to Romaka et al. [31], Co substitution at the Ni site of TiNiSn changed the sign of the Seebeck coefficient above $x \geq 0.03$, indicating that the majority of charge carriers changed to holes. The Seebeck coefficient of 5 % Co-doped TiNiSn is $\approx$ 230 μVK^{-1} at 380 K, which is relatively large among thermoelectric materials, suggesting the possibility of high *ZT*. In addition, according to Wang et al. and Xiong et al., TiNiSn shows higher thermoelectric performance in the P-type than in the N-type in theoretical calculations using first-principles calculations [32,33]. However, there are few reports on the thermoelectric properties of P-type TiNiSn. In addition, to our knowledge, the thermoelectric properties of Co-substituted TiNiSn around 600–800 K, where the peak of *ZT* is expected, have not been experimentally reported.

Therefore, the current study aims to investigate the thermoelectric properties of $TiNi_{1-x}Co_xSn$ ($0 \leq x \leq 0.15$) and find the peak of *ZT* up to 800 K. Our samples with high relative density are prepared by the arc melting method. We also study the variation of structures and electrical transport. Importantly, the optimum stoichiometric ratio to maximize the *ZT* value is reported.

2. Experimental method

2.1. Sample preparation

The raw elements of Ti (grain, 99.9 % up), Ni (grain, 99 %), Co (powder, 99 % up), and Sn (grain, 99.9 % up) were prepared to follow the composition ratio of $TiNi_{1-x}Co_xSn$ (x = 0, 0.01, 0.03, 0.05, 0.08, 0.10, 0.15) so that the total weight is 15 g. The weighed materials were melted in an arc melting furnace with high-purity Ar gas introduced at 5 kPa. Ti for oxygen adsorption getter was melted before the materials to react with the residual air in the melting chamber. In this process, the ingots were flipped and remelted several times on each side. The arc power was gradually increased because if we increase the power too fast, it may cause the material to fly out of the copper heart's mold. Importantly, the distance between the electrode and the sample was carefully controlled to avoid contact. The size of the ingot after arc melting is 13 mm × 35 mm × 7 mm. After arc melting, the samples were cut into measurable dimensions: the size of 7 mm × 7 mm × 1 mm for ρ and *S* measurements, 7 mm × 7 mm × 2 mm for κ measurements (both pellets are cut out from the center of the ingot: cut was started from 5 mm from the edge and 2 mm from the bottom) by a wire electric discharge machine (EC-3025, Makino). The cut samples were vacuum sealed to prevent oxidation and homogenize at 1073 K for 168 h. The carbon sheet was set with the sample in the vacuum-sealed tube to react with residual air. The homogeneity of the pellets is confirmed by powder X-ray diffraction (XRD) and SEM-EDS measurements as shown in the supporting information (Figs. S1–2).

Table 1
Input parameters used for AkaiKKR.

Bravais lattice		fcc
Wyckoff position	Ti	$(x, y, z) = (0, 0, 0)$
	Ni	$(x, y, z) = (0.25, 0.25, 0.25)$
	Sn	$(x, y, z) = (0.5, 0.5, 0.5)$
	Vc	$(x, y, z) = (0.75, 0.75, 0.75)$

2.2. Characterization method

Powder XRD measurements (SmartLab, Rigaku, Cu Kα: λ = 1.5418 Å) were performed to investigate the crystal structure of the samples, and the obtained XRD profiles were used to identify the crystal structure by Rietveld refinement in RIETAN-FP program. The density of samples was measured by the Archimedes method. It was confirmed that high-density samples (6.98–7.20 gcm^{-3} (95%up relative density)) were obtained for all samples. EPMA (JXA-8530F, JEOL Ltd.) was used for compositional analysis. Electrical resistivity and Seebeck coefficient were measured at temperatures ranging from 80 to 395 K using ResiTest8300 (TOYO Co.) and from 395 K to 800 K using home-built apparatus. Thermal conductivity was measured in the range of 300–800 K using a power efficiency measurement system (PEM-2, ULVAC, Inc.). The thermal conductivity of a sample (κ_{sample}) can be determined from the following equation.

$$\kappa_{sample} = \frac{WA}{\Delta T}\frac{1}{\left(\frac{ab}{t}\right)} \quad (1)$$

where *W* is the heat flow density that penetrates the copper block, *A* is the cross-section area of the copper block, ΔT is temperature difference of the sample, and *a*, *b*, and *t* are sample lengths, width, and thickness respectively. To determine the majority of charge carriers, the Hall coefficient was measured at room temperature using ResiTest8300.

First-principles calculations using AkaiKKR [34] were performed by

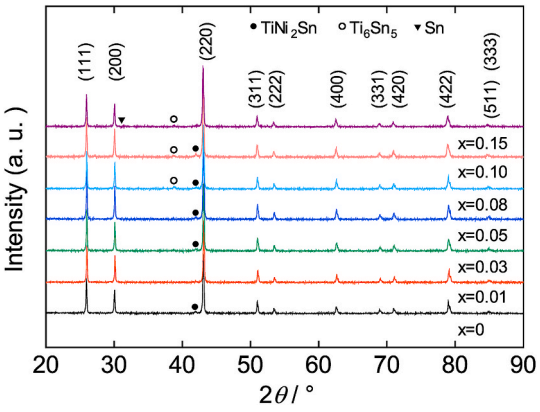

Fig. 2. XRD profiles of $TiNiSn_{1-x}Co_x$ ($0 \leq x \leq 0.15$) at room temperature, where the indexed peaks represent the half-Heusler phase.

changing the occupancies of Ni and Co sites to obtain the density of states near each Fermi level. The crystal structure parameters were taken from the Inorganic Crystal Structure Database (ICSD Code #174568) and the values in Table 1 were used. The generalized gradient approximation (gga91) was used for the exchange correlation term. The convergence condition was set so that the root-mean-square error of the charge density is 1 part per million. The lattice constants were obtained from the Rietveld analysis described below.

3. Result and discussion

Fig. 2 shows the results of powder XRD measurements. The indexed peaks in the figure are the peaks of the half-Heusler (hH) structure. The peaks were observed in all samples, indicating that the prepared samples are composed of Co-doped TiNiSn phase. In addition, a few peaks other than those of the hH phase were observed. These peaks are due to the formation of TiNiSn by the peritectic reaction. It has been reported that they are also formed by other fabrication methods than the arc melting method [35–37]. Those impurity phases are metal, and they are usually not preferable for thermoelectric applications.

The XRD profile after Rietveld analysis is shown in Fig. 3. In the analysis, the Co-doped phase is considered as the main phase, and the multi-phase analysis is performed including impurity phases such as $TiNi_2Sn$, Ti_6Sn_5, and Sn. The crystallographic parameters after the analysis are summarized in Table 2. The reliability factor R_{wp} is less than 10 % for all the samples, and a good refinement of the crystallographic parameters is obtained. The phase fractions indicate that more than 90 % of all samples are Co-doped TiNiSn phase. The x dependence of the lattice parameter after Rietveld analysis is shown in Fig. 4. The $x = 0$ sample shows a larger lattice parameter than the literature value [38], suggesting the presence of point defects [39]. There is little change with increasing x up to $x = 0.08$, but the lattice parameter increases from $x = 0.08$, and from $x = 0.08$ to $x = 0.10$, the lattice parameter increases by 0.01 Å. Since the covalent bond radius of Co is almost the same as that of Ni, the increase in the lattice parameter indicates that there is the presence of point defects (interstitial atoms).

Fig. 5 shows the Back scattered electron (BSE) image for $x = 0.08$. In addition to the Co-doped TiNiSn phase, the presence of impurity phases, which are thought to be $TiNi_2Sn$ and Ti_6Sn_5 phases, is also observed in the XRD profiles above. The compositional analysis shows the averaged results of five measurements of the Co-doped TiNiSn phase. The chemical composition (at%) and actual composition for the Co-doped TiNiSn phase of all samples are shown in Table 3. Table 3 shows that Co is present in the TiNiSn phase in all samples as the nominal composition. In addition, the Ni amount is slightly more than the nominal composition (0.03–0.13), indicating the presence of excess Ni atoms in the TiNiSn phase. Chai et al. reported that TiNiSn tends to produce interstitial Ni atoms and local fH structures, and in this case, the Ni composition ratio is larger than the stoichiometric composition due to the excess of Ni [17]. Therefore, the reason for the increase in the actual composition

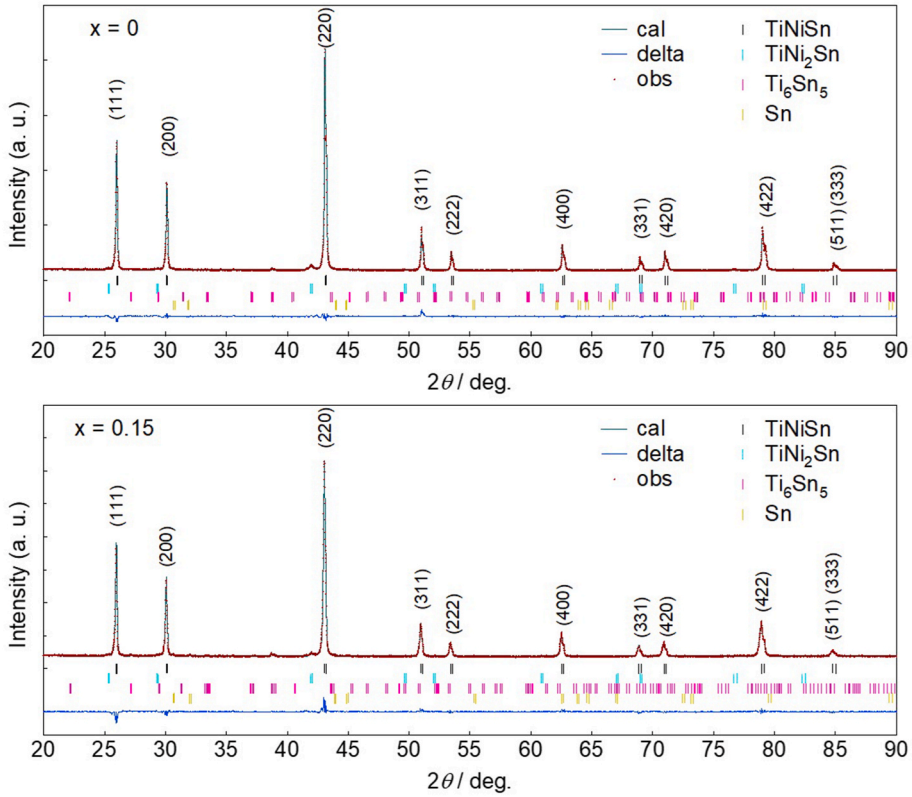

Fig. 3. Rietveld refinement of $TiNi_{1-x}Co_xSn$ ($0 \leq x \leq 0.15$) at diffraction angles of $20° \leq 2\theta \leq 90°$, where the indexed peaks represent the half-Heusler phase.

Table 2
Crystal structure parameters for $TiNi_{1-x}Co_xSn$ ($0 \leq x \leq 0.15$) at room temperature, where the Rietveld analysis refines parameters.

Samples		$TiNi_{1-x}Co_xSn$						
Composition, x		0	0.01	0.03	0.05	0.08	0.10	0.15
Space group		*F3m*						
$a = b = c$ [Å]		5.93307(4)	5.92711(5)	5.93096(5)	5.93086(5)	5.93198(5)	5.93992(7)	5.93877(6)
V [Å^3]		208.85(1)	208.22(1)	208.63(1)	208.62(1)	208.74(1)	209.58(1)	209.45(1)
Ti	x	0	0	0	0	0	0	0
	y	0	0	0	0	0	0	0
	z	0	0	0	0	0	0	0
	B [Å^2]	0.50	0.50	0.50	0.50	0.50	0.50	0.50
	g	1.0	1.0	1.0	1.0	1.0	1.0	1.0
Ni	x	0.25	0.25	0.25	0.25	0.25	0.25	0.25
	y	0.25	0.25	0.25	0.25	0.25	0.25	0.25
	z	0.25	0.25	0.25	0.25	0.25	0.25	0.25
	B [Å^2]	0.50	0.50	0.50	0.50	0.50	0.50	0.50
	g	1.0	0.99	0.97	0.95	0.92	0.90	0.85
Co	x	–	0.25	0.25	0.25	0.25	0.25	0.25
	y	–	0.25	0.25	0.25	0.25	0.25	0.25
	z	–	0.25	0.25	0.25	0.25	0.25	0.25
	B [Å^2]	–	0.50	0.50	0.50	0.50	0.50	0.50
	g	–	0.01	0.03	0.05	0.08	0.10	0.15
Sn	x	0.50	0.50	0.50	0.50	0.50	0.50	0.50
	y	0.50	0.50	0.50	0.50	0.50	0.50	0.50
	z	0.50	0.50	0.50	0.50	0.50	0.50	0.50
	B [Å^2]	0.50	0.50	0.50	0.50	0.50	0.50	0.50
	g	1.0	1.0	1.0	1.0	1.0	1.0	1.0
R_{wp} [%]		3.104	3.456	3.360	3.208	2.961	3.270	3.161
R_P [%]		2.319	2.529	2.509	2.409	2.261	2.446	2.375
R_e [%]		2.121	2.190	2.168	2.148	2.298	2.181	2.137
$S = R_{wp}/R_e$		1.464	1.578	1.549	1.494	1.289	1.499	1.479
R_B [%]		3.213	4.259	3.581	3.484	3.520	5.007	4.995
R_F [%]		1.727	2.026	1.834	1.803	2.077	2.234	2.298
Ti-Ni/Co [Å]		2.5691	2.5665	2.5682	2.5681	2.5686	2.5721	2.5716
Ni/Co-Sn [Å]		2.5691	2.5665	2.5682	2.5681	2.5686	2.5721	2.5716
Sn-Ti [Å]		2.9665	2.9636	2.9655	2.9654	2.9660	2.9700	2.9694
Mass fractions	TiNiSn [%]	94.35	95.11	95.89	97.17	91.56	93.77	95.52
	$TiNi_2Sn$ [%]	3.06	1.48	2.48	1.66	2.11	3.07	1.12
	Ti_6Sn_5 [%]	1.05	1.35	1.23	0.74	5.39	2.61	2.07
	Sn [%]	1.55	2.06	0.40	0.42	0.94	0.55	1.29

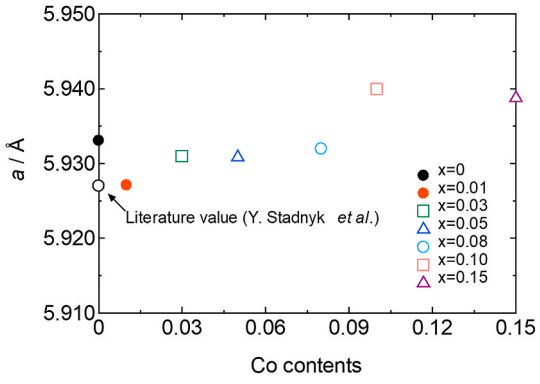

Fig. 4. Lattice constants of $TiNi_{1-x}Co_xSn$ ($0 \leq x \leq 0.15$) depending on Co doping content. The data from the previous report of Stadnyk et al. [38] is included for comparison.

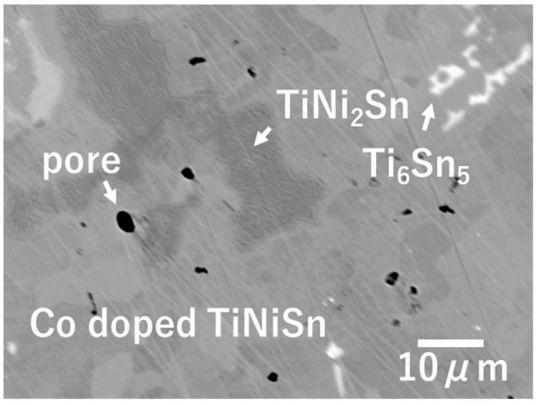

Fig. 5. BSE image obtained from $TiNi_{1-x}Co_xSn$ ($x = 0.08$).

ratio of Ni above the nominal composition may be attributed to these factors.

The values of Hall coefficient R_H [cm^{3}C^{-1}], Hall carrier density n_H [cm^{-3}], Hall mobility μ_H [cm^{2}V^{-1}s^{-1}], and thermoelectric properties at room temperature obtained from Hall effect measurements are summarized in Table 4. For $x \geq 0.03$, the sign of Hall coefficient changed from negative to positive, indicating that the majority of charge carriers changed from electrons (N-type) to holes (P-type). The dependence of Hall carrier density on the amount of Co substitution is shown in Fig. 6.

The Hall carrier density increases with increasing x. Since the Hall carrier density does not increase beyond 5.0×10^{21} cm^{-3}, it is considered that based on the results of the lattice parameter changes described above, this may be due to the formation of point defects (interstitial atoms), resulting in saturation of the hole density. Fig. 7 shows the Hall mobility as a function of x. The Hall mobility decreases by more than one order of magnitude after the change of majority carriers. The mobility can be expressed in terms of the relaxation time τ, the effective mass m^*, and the electric charge q by the following equation

Table 3
Elemental composition of $TiNi_{1-x}Co_xSn$ ($0 \leq x \leq 0.15$) at room temperature which is determined by quantitative analysis using EPMA.

x	Chemical composition (at%)				Actual composition for Co-doped TiNiSn phase
	Ti	Ni	Co	Sn	
0	32.8 (1)	34.4 (2)	–	32.8 (1)	$Ti_{0.999(4)}Ni_{1.05(1)}Sn_{1.00(1)}$
0.01	33.1 (1)	33.7 (1)	0.30 (4)	32.8 (1)	$Ti_{1.00(1)}Ni_{1.02(1)}Co_{0.009(1)}Sn_{0.995(3)}$
0.03	33.0 (2)	33.6 (3)	0.92 (7)	32.5 (1)	$Ti_{1.01(1)}Ni_{1.02(1)}Co_{0.028(2)}Sn_{0.993(4)}$
0.05	32.5 (1)	32.9 (1)	1.7(1)	32.9 (2)	$Ti_{0.994(3)}Ni_{1.00(1)}Co_{0.051(2)}Sn_{1.01(1)}$
0.08	32.5 (1)	32.5 (3)	2.8(2)	32.1 (1)	$Ti_{1.01(1)}Ni_{1.01(1)}Co_{0.088(5)}Sn_{0.993(4)}$
0.10	32.4 (2)	32.2 (3)	3.3(1)	32.0 (1)	$Ti_{1.01(1)}Ni_{1.00(1)}Co_{0.10(1)}Sn_{0.994(2)}$
0.15	32.0 (5)	31.3 (2)	4.8(8)	31.8 (3)	$Ti_{1.00(2)}Ni_{0.980(5)}Co_{0.15(2)}Sn_{1.00(1)}$

$$\mu = \frac{q\tau}{m^*} \tag{2}$$

From Eq. (2), if the effective mass of the electron is m_e^* and that of the hole is m_h^*, then $m_h^* > m_e^*$, which explains the decrease in mobility after the majority of charge carriers changes. The Hall mobility decreases with the increase of x. In addition, since the presence of point defects also decreases the mobility, the low Hall mobility is also due to point defects.

Fig. 8 shows the temperature dependence of electrical resistivity ρ [Ωcm]. Above room temperature, a semiconducting behavior is observed in which the electrical resistivity decreases with increasing temperature for all samples. ρ has the following relationship with electric charge q, carrier density n, and mobility μ.

$$\rho = \frac{1}{qn\mu} \tag{3}$$

After the majority of charge carriers change, the electrical resistivity increases more than $x = 0$ up to $x \leq 0.05$, because the mobility decreases by more than one order of magnitude. For $x \geq 0.08$, the Hall carrier density reaches the region of degenerate semiconductors and the electrical resistivity decreases.

Fig. 9 shows the temperature dependence of the Seebeck coefficient S [μVK^{-1}]. The highest Seebeck coefficient for $x = 0.05$ was observed for the prepared samples. Consistent with the Hall effect measurements, the Seebeck coefficient changes its sign for $x \geq 0.03$. For $x = 0.01$, the Seebeck coefficient is positive up to around room temperature but turns negative with increasing temperature due to the effect of excited carriers, as the majority of charge carriers changes from holes to electrons. Since the absolute value of the Seebeck coefficient decreases for $x > 0.05$, excessive Co substitution decreases the absolute value of the Seebeck coefficient. For this reason, according to Mott's equation, the Seebeck coefficient can be expressed as follows [40–42].

$$|S| \approx \frac{{k_B}^2}{3|e|} T \frac{m^*}{\hbar^2} \left(\frac{\pi}{3n}\right)^{\frac{2}{3}} \tag{4}$$

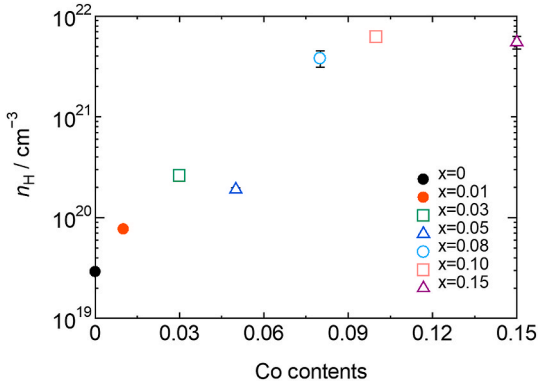

Fig. 6. x dependence of Hall carrier density (n_H) for $TiNi_{1-x}Co_xSn$ ($0 \leq x \leq 0.15$) at room temperature.

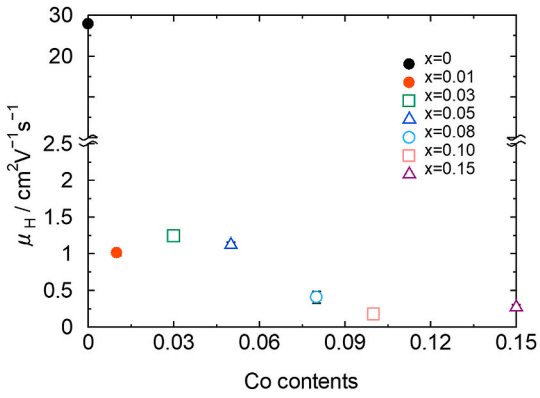

Fig. 7. x dependence of Hall mobility (μ_H) for $TiNi_{1-x}Co_xSn$ ($0 \leq x \leq 0.15$) at room temperature.

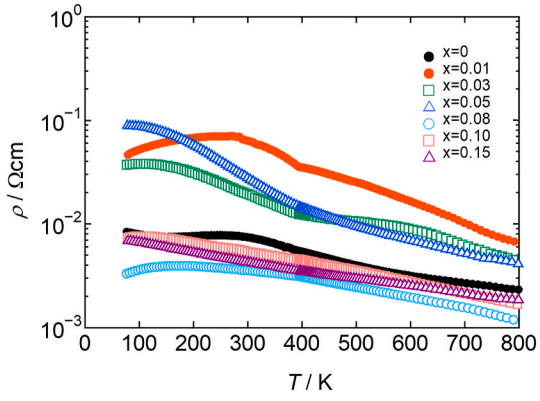

Fig. 8. Temperature dependence of electrical resistivity (ρ) for $TiNi_{1-x}Co_xSn$ ($0 \leq x \leq 0.15$).

Table 4
Summary of thermoelectric properties of $TiNi_{1-x}Co_xSn$ ($0 \leq x \leq 0.15$) at room temperature, where L_0, n_H, μ_H, S, ρ, and κ are Lorenz number, Hall carrier density, Hall mobility, Seebeck coefficient, electrical resistivity, and total thermal conductivity, respectively.

x	L_0 [$\times 10^{-8}$ V^2K^{-2}]	R_H [cm^3C^{-1}]	n_H [cm^{-3}]	μ_H [$cm^2V^{-1}s^{-1}$]	$\lvert S\rvert$ [μVK^{-1}]	ρ [Ωcm]	κ [$Wm^{-1}K^{-1}$]
0	1.629	$-2.12\ (2) \times 10^{-1}$	$2.9\ (1) \times 10^{19}$	28(1)	273	7.38×10^{-3}	5.44
0.01	2.440	$-8.1\ (3) \times 10^{-2}$	$7.7\ (3) \times 10^{19}$	1.0(1)	5.09	6.31×10^{-2}	5.81
0.03	1.967	$2.5\ (1) \times 10^{-2}$	$2.6\ (1) \times 10^{20}$	1.2(1)	89.4	1.95×10^{-2}	4.07
0.05	1.658	$3.2\ (1) \times 10^{-2}$	$1.9\ (1) \times 10^{20}$	1.1(1)	192	2.78×10^{-2}	4.73
0.08	2.336	$1.7\ (3) \times 10^{-3}$	$3.8\ (7) \times 10^{21}$	0.41 (8)	33.0	3.54×10^{-3}	3.66
0.10	2.352	$1.0\ (1) \times 10^{-3}$	$6.2\ (1) \times 10^{21}$	0.17(1)	30.3	5.37×10^{-3}	3.50
0.15	2.310	$1.2\ (2) \times 10^{-3}$	$5.5\ (8) \times 10^{21}$	0.27(4)	36.9	4.26×10^{-3}	3.76

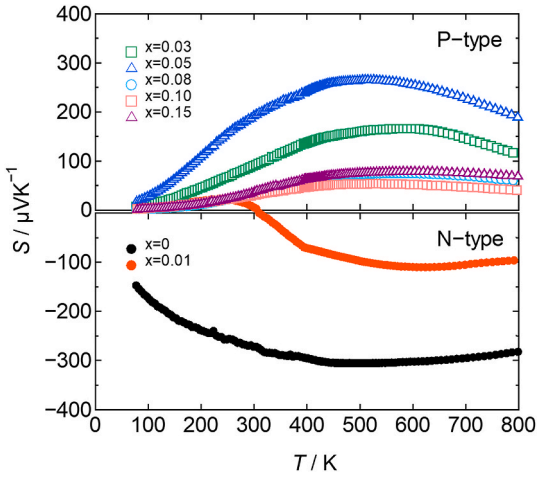

Fig. 9. Temperature dependence of the Seebeck coefficient (S) for $TiNi_{1-x}Co_xSn$ ($0 \leq x \leq 0.15$).

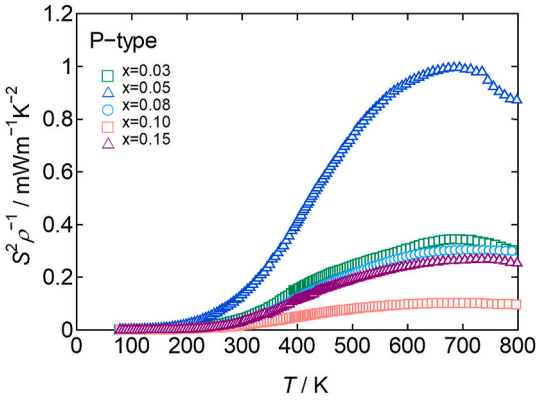

Fig. 10. Temperature dependence of power factor ($S^2\rho^{-1}$) for $TiNi_{1-x}Co_xSn$ ($0 \leq x \leq 0.15$).

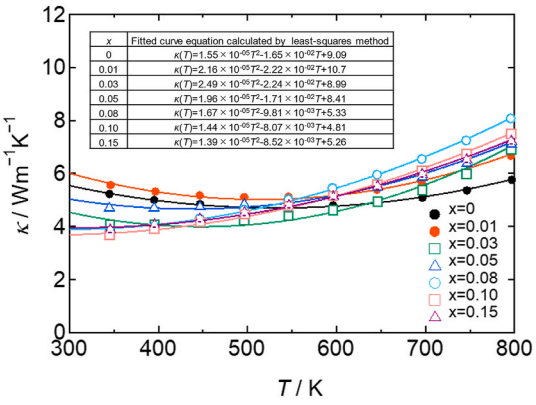

Fig. 11. Temperature dependence of total thermal conductivity ($\kappa = \kappa_{el} + \kappa_{lat}$) for $TiNi_{1-x}Co_xSn$ ($0 \leq x \leq 0.15$), inset is fitted curve equation calculated by least-squares method.

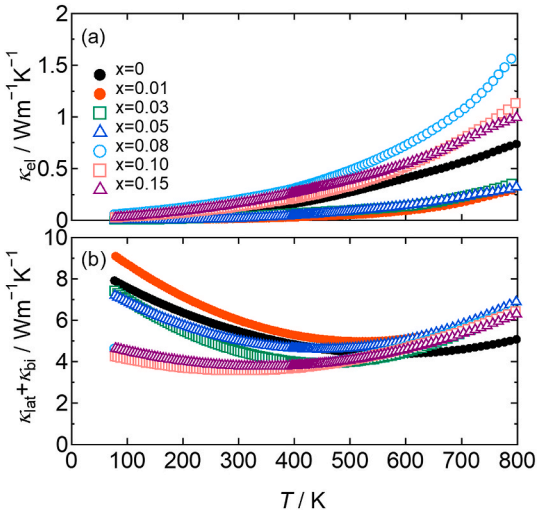

Fig. 12. (a) Temperature dependence of carrier thermal conductivity (κ_{el}) for $TiNi_{1-x}Co_xSn$ ($0 \leq x \leq 0.15$). where $\kappa_{el} = L_0\rho^{-1}T$ calculated by Wiedemann-Franz law. (b) Temperature dependence of lattice thermal conductivity and bipolar thermal conductivity ($\kappa_{lat} + \kappa_{bi} = \kappa - \kappa_{el}$) for $TiNi_{1-x}Co_xSn$ ($0 \leq x \leq 0.15$).

where k_B is Boltzmann constant, e is the elementary charge, $\hbar$ is Planck constant, n is carrier density, and m^* is the effective mass. From Eq. (4), $x > 0.05$ can be explained by the fact that the absolute value of the Seebeck coefficient decreases because the carrier density increases by more than one order of magnitude. Since the effective mass and mobility are inversely related, the effective mass is expected to increase with increasing x. However, in the temperature range measured, the absolute Seebeck coefficient is dominated by the carrier density rather than the increase in effective mass. Table 3 shows that all samples exhibit excess Ni composition ratios, suggesting the presence of interstitial Ni atoms or local fH phases. According to Ren et al., the presence of interstitial Ni atoms decreases the Seebeck coefficient $|S|$ [39]. This effect was reported not only for TiNiSn but also for ZrNiSn, which is also a half-Heusler alloy [43]. Therefore, excess Ni atoms may decrease the absolute value of the Seebeck coefficient. Since interstitial Ni atoms and local fH phases are formed during the reaction process, control of excess Ni atoms requires off-stoichiometric composition control. The control of excess Ni atoms is expected to suppress the decrease of the Seebeck coefficient.

Fig. 10 shows the power factor $S^2\rho^{-1}$ [$mWm^{-1}K^{-2}$] for $x \geq 0.03$, which is P-type. The power factor shows a maximum at $x = 0.05$, which is attributed to the Seebeck coefficient $|S|$ being the largest among the P-type samples. For $x > 0.05$, the carrier density increases by an order of magnitude, and the Seebeck coefficient $|S|$ decreases, so that the optimum carrier density is estimated to be around $\approx 10^{20}$ cm^{-3}.

Fig. 11 shows the temperature dependence of thermal conductivity κ [$Wm^{-1}K^{-1}$]. κ were measured in the 300–800 K range. Outside the measurement range was extrapolated by the least-squares method. The fitted curve equations are shown in the inset figure. After Co substitution, the temperature dependence of the high-temperature thermal conductivity changes. For $x \geq 0.01$, the thermal conductivity increases by about 0.5–2 $Wm^{-1}K^{-1}$ at high temperatures. From the Wiedemann-Franz law, the carrier thermal conductivity is obtained by the following equation

$$\kappa_{el} = \frac{L_0 T}{\rho} \tag{5}$$

where L_0 [V^2K^{-2}] is the Lorenz number, and the value of the Lorenz number is determined from the experimental values of the Seebeck coefficient at room temperature using the following equation [44]. The scattering factor r is assumed to be acoustic phonon scattering, and $r = -1/2$ is used [45].

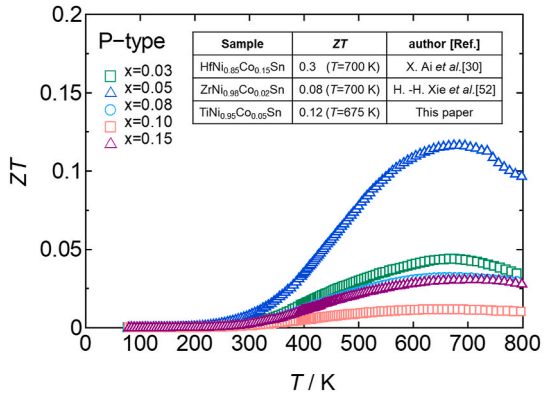

Sample	ZT	author [Ref.]
$HfNi_{0.85}Co_{0.15}Sn$	0.3 (T=700 K)	X. Ai *et al.*[30]
$ZrNi_{0.98}Co_{0.02}Sn$	0.08 (T=700 K)	H. -H. Xie *et al.*[52]
$TiNi_{0.95}Co_{0.05}Sn$	0.12 (T=675 K)	This paper

Fig. 13. Temperature dependence of ZT for $TiNi_{1-x}Co_xSn$ ($0 \leq x \leq 0.15$), inset is ZT values of previous studies for $HfNi_{0.85}Co_{0.15}Sn$ [30], $ZrNi_{0.98}Co_{0.02}Sn$ [52], and that of our research for $TiNi_{0.95}Co_{0.05}Sn$.

$$L_0 = \left(\frac{k_B}{e}\right)^2 \left\{ \frac{\left(r+\frac{7}{2}\right)F_{r+\frac{5}{2}}(\eta)}{\left(r+\frac{3}{2}\right)F_{r+\frac{1}{2}}(\eta)} - \left[\frac{\left(r+\frac{5}{2}\right)F_{r+\frac{3}{2}}(\eta)}{\left(r+\frac{3}{2}\right)F_{r+\frac{1}{2}}(\eta)} \right]^2 \right\} \tag{6}$$

where $F_n(\eta)$ is a function of the Fermi energy E_F with the following relation.

$$F_n(\eta) = \int_0^\infty \frac{\chi^n}{1+e^{\chi-\eta}} d\chi \tag{7}$$

$$\eta = \frac{E_F}{k_B T} \tag{8}$$

Table 4 summarizes the Lorenz number for each sample. Fig. 12 shows the carrier thermal conductivity calculated from equation (5), also the temperature dependence of the lattice thermal conductivity and the bipolar thermal conductivity due to minority carriers (κ_{bi}), which is the thermal conductivity minus the carrier thermal conductivity.

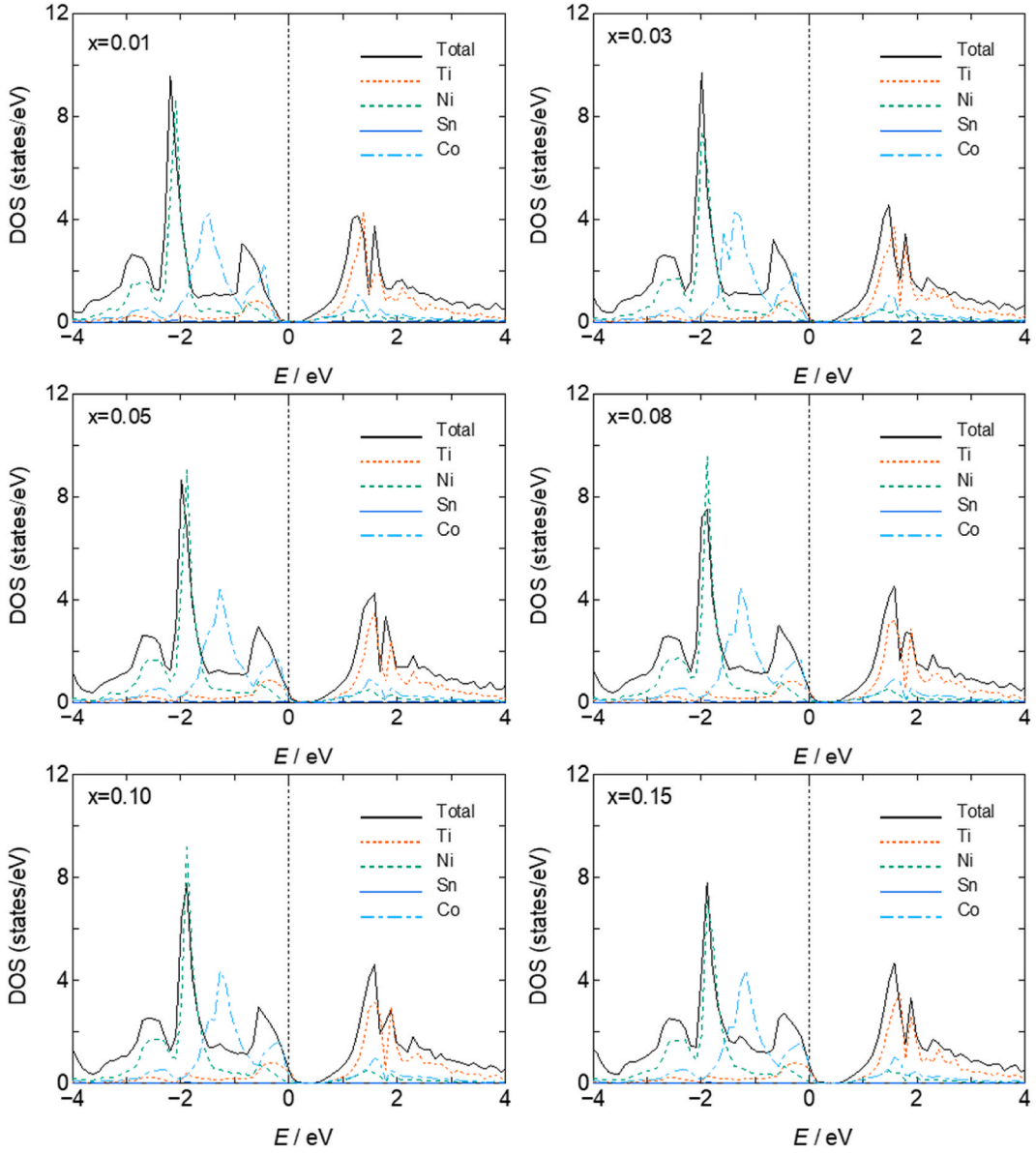

Fig. 14. DOS calculated by AkaiKKR for $TiNi_{1-x}Co_xSn$ ($0 \leq x \leq 0.15$) near the Fermi level.

From Fig. 12, the sample with a large carrier density $x \geq 0.08$ shows 1.0–1.6 $Wm^{-1}K^{-1}$ at high temperatures. The thermal conductivity of the samples with large carrier density increases at high temperatures due to significant carrier excitation. And the lattice thermal conductivity dominates the thermal conductivity of Co-substituted TiNiSn. This result also indicates that the decrease in lattice thermal conductivity is effective in reducing total thermal conductivity [46]. In general, the lattice thermal conductivity decreases after the Debye temperature. Since the Debye temperature of TiNiSn is around ≈400 K [47–50], the rise in the high temperature is due to the effect of minority carriers (bipolar effect) [51]. Therefore, the increase of thermal conductivity at high temperatures for $x \geq 0.01$ is due to the effects of both electron and hole carriers.

Using the results for S, ρ, and κ (80–300 K are extrapolated values), we calculated ZT. Fig. 13 shows the temperature dependence of ZT. The largest ZT is obtained for $x = 0.05$, showing $ZT = 0.12$ at $T = 675$K. The large ZT is attributed to the high-power factor. In addition, for $x \geq 0.08$, the absolute value of the Seebeck coefficient decreases and ZT deteriorates due to the increase of thermal conductivity at the high temperature. The inset compares these results with those of a previous study of Co-doping in a similar half-Heusler MNiSn (M = Ti, Zr, Hf) at similar temperatures. The ZT of our study's value is inferior to that of HfNiSn, which is composed of expensive Hf, but larger than that of ZrNiSn.

Fig. 14 shows the density of states (DOS) near the Fermi level of $TiNi_{1-x}Co_xSn$ ($0 \leq x \leq 0.15$) using AkaiKKR. The dotted line in the center indicates the Fermi level. With increasing Co substitution, the Fermi level shifts toward the valence band. This is considered to be due to the formation of an acceptor level by Co, and first-principles calculations also indicate that the Co substitution at the Ni site is effective in making TiNiSn P-type. The change in the number of carriers associated with the shift of the Fermi level is consistent with the experimental results. The Hall effect measurements show that the carrier density increases up to the region of degenerate semiconductors for $x \geq 0.08$, but the ab initio calculations suggest that the increase in carrier density is due to the Fermi level entering into the valence band and becoming degenerate.

4. Conclusion

In this study, thermoelectric properties of P-type half-Heusler $TiNi_{1-x}Co_xSn$ ($0 \leq x \leq 0.15$) were measured up to 800 K to clarify the ZT at the high-temperature side. From the Hall effect measurements and Seebeck coefficient measurements, we confirmed the change of majority carriers in TiNiSn for $x \geq 0.03$. This result is consistent with the results reported by Romaka et al. [27] and first-principles calculations and confirms that Co substitution at Ni sites is effective for hole doping. As for ZT, $x = 0.05$ ($Ti_{0.994}Ni_{1.00}Co_{0.051}Sn_{1.01}$) showed the largest ZT value ($ZT = 0.12$, $T = 675$ K) among all P-type samples. The results of the compositional analysis indicated the presence of excess Ni atoms in the Co-doped TiNiSn phase. The presence of excess Ni atoms possibly provokes a decrease in the Seebeck coefficient; however, this could be improved by controlling the Ni compositional ratio. As a prospect, further increase of ZT can be expected by controlling the excess Ni atoms and by reducing the lattice thermal conductivity through heavy elements substitution.

CRediT authorship contribution statement

Kosuke Yamazaki: Writing – original draft, Visualization, Methodology, Investigation, Formal analysis, Data curation, Conceptualization. **Sopheap Sam:** Writing – review & editing. **Yoichi Okamoto:** Resources, Conceptualization. **Hiroshi Nakatsugawa:** Validation, Supervision, Software, Project administration, Funding acquisition.

Declaration of competing interest

The authors declare that they have no known competing financial interests or personal relationships that could have appeared to influence the work reported in this paper.

Data availability

Data will be made available on request.

Acknowledgments

XRD and EPMA measurements were conducted using the equipment of the Instrumental Analysis Center, at Yokohama National University. PEM-2 was performed at the National Defense Academy of Japan. In addition, the authors would like to express appreciation to Mr. Hiromichi Togashi for cooperating with sample preparation and measurement of thermoelectric properties at 80–395 K for this study.

Appendix A. Supplementary data

Supplementary data to this article can be found online at https://doi.org/10.1016/j.solidstatesciences.2024.107708.

References

[1] R. Ovik Fitriani, B.D. Long, M.C. Barma, M. Riaz, M.F.M. Sabri, S.M. Said, R. Saidur, A review on nanostructures of high-temperature thermoelectric materials for waste heat recovery, Renew. Sustain. Energy Rev. 64 (2016) 635–659, https://doi.org/10.1016/j.rser.2016.06.035.
[2] H. Jouhara, N. Khordehgah, S. Almahmoud, B. Delpech, A. Chauhan, S.A. Tassou, Waste heat recovery technologies and applications, Therm. Sci. Eng. Prog. 6 (2018) 268–289, https://doi.org/10.1016/j.tsep.2018.04.017.
[3] G. Min, D.M. Rowe, Optimisation of thermoelectric module geometry for "waste heat" electric power generation, J. Power Sources 38 (1992) 253–259.
[4] D.M. Rowe, G. Min, Evaluation of thermoelectric modules for power generation, J. Power Sources 73 (1998) 193–198.
[5] J.R. Sootsman, D.Y. Chung, M.G. Kanatzidis, New and old concepts in thermoelectric materials, Angewandte Chemie - International Edition 48 (2009) 8616–8639, https://doi.org/10.1002/anie.200900598.
[6] J. Wei, L. Yang, Z. Ma, P. Song, M. Zhang, J. Ma, F. Yang, X. Wang, Review of current high-ZT thermoelectric materials, J. Mater. Sci. 55 (2020) 12642–12704, https://doi.org/10.1007/s10853-020-04949-0.
[7] I. Terasaki, Y. Sasago, K. Uchinokura, Large thermoelectric power in NaCo2O4 single crystals, Phys. Rev. B Condens. Matter 56 (1997) 12685.
[8] G. Ren, J. Lan, C. Zeng, Y. Liu, B. Zhan, S. Butt, Y.H. Lin, C.W. Nan, High performance oxides-based thermoelectric materials, JOM 67 (2015) 211–221, https://doi.org/10.1007/s11837-014-1218-2.
[9] A.V. Powell, Recent developments in Earth-abundant copper-sulfide thermoelectric materials, J. Appl. Phys. 126 (2019), https://doi.org/10.1063/1.5119345.
[10] P. Jood, M. Ohta, Hierarchical architecturing for layered thermoelectric sulfides and chalcogenides, Materials 8 (2015) 1124–1149, https://doi.org/10.3390/ma8031124.
[11] A. Nozariasbmarz, A. Agarwal, Z.A. Coutant, M.J. Hall, J. Liu, R. Liu, A. Malhotra, P. Norouzzadeh, M.C. Öztürk, V.P. Ramesh, Y. Sargolzaeiaval, F. Suarez, D. Vashaee, Thermoelectric silicides: a review, Jpn. J. Appl. Phys. 56 (2017), https://doi.org/10.7567/JJAP.56.05DA04.
[12] A.T. Burkov, Silicide thermoelectrics: materials for energy harvesting, Physica Status Solidi (A) Applications and Materials Science 215 (2018), https://doi.org/10.1002/pssa.201800105.
[13] T. Zhu, C. Fu, H. Xie, Y. Liu, X. Zhao, High efficiency half-heusler thermoelectric materials for energy harvesting, Adv. Energy Mater. 5 (2015), https://doi.org/10.1002/aenm.201500588.
[14] L. Huang, Q. Zhang, B. Yuan, X. Lai, X. Yan, Z. Ren, Recent progress in half-Heusler thermoelectric materials, Mater. Res. Bull. 76 (2016) 107–112, https://doi.org/10.1016/j.materresbull.2015.11.032.
[15] G. Rogl, A. Grytsiv, M. Gürth, A. Tavassoli, C. Ebner, A. Wünschek, S. Puchegger, V. Soprunyuk, W. Schranz, E. Bauer, H. Müller, M. Zehetbauer, P. Rogl, Mechanical properties of half-Heusler alloys, Acta Mater. 107 (2016) 178–195, https://doi.org/10.1016/j.actamat.2016.01.031.
[16] K. Kurosaki, Y. Ohishi, H. Muta, S. Yamanaka, Half-Heusler compounds as promising high-performance thermoelectric materials, Netsu Sokutei 43 (2016), 2016–2016.
[17] Y. Wang Chai, Y. Kimura, Nanosized precipitates in half-Heusler TiNiSn alloy, Appl. Phys. Lett. 100 (2012), https://doi.org/10.1063/1.3679377.
[18] K. Kirievsky, M. Shlimovich, D. Fuks, Y. Gelbstein, An ab initio study of the thermoelectric enhancement potential in nano-grained TiNiSn, Phys. Chem. Chem. Phys. 16 (2014) 20023–20029, https://doi.org/10.1039/c4cp02868f.
[19] M. Rittiruam, A.A.B. Padama, A. Vora-Ud, A. Yangthaisong, T. Seetawan, W. A. Diño, Dilute concentrations of Sb (Bi) dopants in Sn-site enhance the thermoelectric properties of TiNiSn half-Heusler alloys: a first-principles study, Jpn. J. Appl. Phys. 59 (2020), https://doi.org/10.35848/1347-4065/ab74c8.

[20] T.M. Tritt, Holey and unholey semiconductors, Science 283 (1979) 804–805, https://doi.org/10.1126/science.283.5403.804, 1999.
[21] S. Bhattacharya, A.L. Pope, R.T. Littleton IV, T.M. Tritt, V. Ponnambalam, Y. Xia, S. J. Poon, Effect of Sb doping on the thermoelectric properties of Ti-based half-Heusler compounds, TiNiSn1-xSbx, Appl. Phys. Lett. 77 (2000) 2476–2478, https://doi.org/10.1063/1.1318237.
[22] K. Yamazaki, H. Nakatsugawa, Y. Okamoto, Thermoelectric properties and electric structure of Sb substituted TiNiSn half-Heusler alloys, The Journal of the Thermoelectrics Society of Japan 20 (2023) 75–81, https://doi.org/10.50972/thermoelectrics.20.2_75.
[23] K. Chen, C. Nuttall, E. Stefanaki, K. Placha, R. Tuley, K. Simpson, J.W.G. Bos, M. J. Reece, Fast synthesis of n-type half-heusler TiNiSn thermoelectric material, Scr Mater 191 (2021) 71–75, https://doi.org/10.1016/j.scriptamat.2020.09.010.
[24] S.W. Kim, Y. Kimura, Y. Mishima, High temperature thermoelectric properties of TiNiSn-based half-Heusler compounds, Intermetallics 15 (2007) 349–356, https://doi.org/10.1016/j.intermet.2006.08.008.
[25] V.A. Romaka, P. Rogl, V.V. Romaka, E.K. Hlil, Y.V. Stadnyk, S.M. Budgerak, Features of a priori heavy doping of the n-TiNiSn intermetallic semiconductor, Semiconductors 45 (2011) 850–856, https://doi.org/10.1134/S1063782611070190.
[26] L. Romaka, Y. Stadnyk, A. Horyn, M.G. Shelyapina, V.S. Kasperovich, D. Fruchart, E.K. Hlil, P. Wolfers, Electronic structure of the Ti1-xScxNiSn and Zr1-xScxNiSn solid solutions, J. Alloys Compd. 396 (2005) 64–68, https://doi.org/10.1016/j.jallcom.2004.12.034.
[27] V.A. Romaka, Yu V. Stadnyk, D. Fruchart, T.I. Dominuk, L.P. Romaka, P. Rogl, A. M. Goryn, The mechanism of generation of the donor- and acceptor-type defects in the n-TiNiSn semiconductor heavily doped with Co impurity, Semiconductors 43 (2009) 1124–1130, https://doi.org/10.1134/s1063782609090036.
[28] S. Katsuyama, H. Matsushima, M. Ito, Effect of substitution for Ni by Co and/or Cu on the thermoelectric properties of half-Heusler ZrNiSn, J. Alloys Compd. 385 (2004) 232–237, https://doi.org/10.1016/j.jallcom.2004.02.061.
[29] Y. Kimura, T. Tanoguchi, T. Kita, Vacancy site occupation by Co and Ir in half-Heusler ZrNiSn and conversion of the thermoelectric properties from n-type to p-type, Acta Mater. 58 (2010) 4354–4361, https://doi.org/10.1016/j.actamat.2010.04.028.
[30] X. Ai, B. Lei, M.O. Cichocka, L. Giebeler, R.B. Villoro, S. Zhang, C. Scheu, N. Pérez, Q. Zhang, A. Sotnikov, D.J. Singh, K. Nielsch, R. He, Enhancing the thermoelectric properties via modulation of defects in P-type MNiSn-based (M = Hf, Zr, Ti) half-heusler materials, Adv. Funct. Mater. 33 (2023), https://doi.org/10.1002/adfm.202305582.
[31] V.A. Romaka, Yu V. Stadnyk, D. Fruchart, T.I. Dominuk, L.P. Romaka, P. Rogl, A. M. Goryn, The mechanism of generation of the donor- and acceptor-type defects in the n-TiNiSn semiconductor heavily doped with Co impurity, Semiconductors 43 (2009) 1124–1130, https://doi.org/10.1134/s1063782609090036.
[32] L.L. Wang, L. Miao, Z.Y. Wang, W. Wei, R. Xiong, H.J. Liu, J. Shi, X.F. Tang, Thermoelectric performance of half-Heusler compounds TiNiSn and TiCoSb, J. Appl. Phys. 105 (2009), https://doi.org/10.1063/1.3056384.
[33] M. Xiong, S. Yang, First-principles study on the lattice dynamics, electronic, mechanical, and thermoelectric properties of half-heusler compounds TiXSn (X = Ni, Pd, Pt), Mater. Today Commun. 38 (2024), https://doi.org/10.1016/j.mtcomm.2024.108051.
[34] H. Akai, Electronic structure Ni–Pd alloys calculated by the self-consistent KKR-CPA method, J Physical Soc Japan 51 (1982) 468–474, https://doi.org/10.1143/JPSJ.51.468.
[35] M. Gürth, A. Grytsiv, J. Vrestal, V.V. Romaka, G. Giester, E. Bauer, P. Rogl, On the constitution and thermodynamic modelling of the system Ti-Ni-Sn, RSC Adv. 5 (2015) 92270–92291, https://doi.org/10.1039/c5ra16074j.
[36] M. Tillard, A. Berche, P. Jund, Synthesis of pure NiTiSn by mechanical alloying: an investigation of the optimal experimental conditions supported by first principles calculations, Metals 8 (2018), https://doi.org/10.3390/met8100835.
[37] T. Katayama, S.W. Kim, Y. Kimura, Y. Mishima, The effects of quaternary additions on thermoelectric properties of TiNiSn-based half-heusler alloys, J. Electron. Mater. 32 (2003).
[38] Y. Stadnyk, A. Horyn, V.V. Romaka, Y. Gorelenko, L.P. Romaka, E.K. Hlil, D. Fruchart, Crystal, electronic structure and electronic transport properties of the Ti1-xVxNiSn (x=0-0.10) solid solutions, J. Solid State Chem. 183 (2010) 3023–3028, https://doi.org/10.1016/j.jssc.2010.09.042.
[39] W. Ren, H. Zhu, J. Mao, L. You, S. Song, T. Tong, J. Bao, J. Luo, Z. Wang, Z. Ren, Manipulation of Ni interstitials for realizing large power factor in TiNiSn-based materials, Adv Electron Mater 5 (2019), https://doi.org/10.1002/aelm.201900166.
[40] N.F. Mott, H. Jones, The Theory of the Properties of Metals and Alloys, Clarendon, Oxford, 1936.
[41] J.M. Ziman, Electrons and Phonons, Oxford University press, England, 1960.
[42] N.W. Ashcroft, N.D. Mermin, Solid State Physics, Saunders Colledge Publishers, Philadelphia, 1976.
[43] C. Fu, M. Yao, X. Chen, L.Z. Maulana, X. Li, J. Yang, K. Imasato, F. Zhu, G. Li, G. Auffermann, U. Burkhardt, W. Schnelle, J. Zhou, T. Zhu, X. Zhao, M. Shi, M. Dressel, A.V. Pronin, G.J. Snyder, C. Felser, Revealing the intrinsic electronic structure of 3D half-heusler thermoelectric materials by angle-resolved photoemission spectroscopy, Adv. Sci. 7 (2020), https://doi.org/10.1002/advs.201902409.
[44] L.D. Zhao, S.H. Lo, J. He, H. Li, K. Biswas, J. Androulakis, C.I. Wu, T.P. Hogan, D. Y. Chung, V.P. Dravid, M.G. Kanatzidis, High performance thermoelectrics from earth-abundant materials: enhanced figure of merit in PbS by second phase nanostructures, J. Am. Chem. Soc. 133 (2011) 20476–20487, https://doi.org/10.1021/ja208658w.
[45] L.D. Zhao, B.P. Zhang, W.S. Liu, J.F. Li, Effect of mixed grain sizes on thermoelectric performance of Bi2Te3 compound, J. Appl. Phys. 105 (2009), https://doi.org/10.1063/1.3063694.
[46] S.R. Culp, J.W. Simonson, S.J. Poon, V. Ponnambalam, J. Edwards, T.M. Tritt, (Zr, Hf)Co(Sb,Sn) half-Heusler phases as high-temperature (>700 °c) p -type thermoelectric materials, Appl. Phys. Lett. 93 (2008), https://doi.org/10.1063/1.2959103.
[47] M. Rittiruam, A. Yangthaisong, T. Seetawan, Reduced lattice thermal conductivity of Ti-site substituted transition metals Ti1-XTMXNiSn: a quasi-harmonic Debye model study, Chin. J. Phys. 57 (2019) 393–402, https://doi.org/10.1016/j.cjph.2018.10.029.
[48] C. Toher, J.J. Plata, O. Levy, M. De Jong, M. Asta, M.B. Nardelli, S. Curtarolo, High-throughput computational screening of thermal conductivity, Debye temperature, and Grüneisen parameter using a quasiharmonic Debye model, Phys Rev B Condens Matter Mater Phys 90 (2014), https://doi.org/10.1103/PhysRevB.90.174107.
[49] A. Page, C. Uher, P.F. Poudeu, A. Van Der Ven, Phase separation of full-Heusler nanostructures in half-Heusler thermoelectrics and vibrational properties from first-principles calculations, Phys Rev B Condens Matter Mater Phys 92 (2015), https://doi.org/10.1103/PhysRevB.92.174102.
[50] R. Kuentzler, R. Clad, G. Schmcrber, Y. Dossmann, Gap at the Fermi level and magnetism in RMSn ternary compounds (R=Ti, Zr, Hf and M=Fe, Co, Ni), J. Magn. Magn Mater. 104–107 (1992) 1976–1978.
[51] T. Berry, S. Ouardi, G.H. Fecher, B. Balke, G. Kreiner, G. Auffermann, W. Schnelle, C. Felser, Improving thermoelectric performance of TiNiSn by mixing MnNiSb in the half-Heusler structure, Phys. Chem. Chem. Phys. 19 (2017) 1543–1550, https://doi.org/10.1039/c6cp06859f.
[52] H.H. Xie, C. Yu, B. He, T.J. Zhu, X.B. Zhao, Thermoelectric properties and n- to p-type conversion of Co-doped ZrNiSn-based half-heusler alloys, J. Electron. Mater. 41 (2012) 1826–1830, https://doi.org/10.1007/s11664-012-2077-7.